Applied Physics Letters

# Double-shell interphase design enabling suppressed side reactions for stable Si battery anode

Cite as: Appl. Phys. Lett. **121**, 123905 (2022); https://doi.org/10.1063/5.0117229
Submitted: 31 July 2022 • Accepted: 04 September 2022 • Published Online: 22 September 2022

**Xiaoxue Chen, Zihe Chen, Yang Ni, et al.**

AIP Publishing

Applied Physics Letters ARTICLE scitation.org/journal/apl

# Double-shell interphase design enabling suppressed side reactions for stable Si battery anode

Cite as: Appl. Phys. Lett. **121**, 123905 (2022); doi: 10.1063/5.0117229
Submitted: 31 July 2022 · Accepted: 4 September 2022 ·
Published Online: 22 September 2022

Xiaoxue Chen,[1] Zihe Chen,[1] Yang Ni,[2] Li Wang,[3,a)] and Yongming Sun[1,a)]

AFFILIATIONS

[1]Wuhan National Laboratory for Optoelectronics, Huazhong University of Science and Technology, Wuhan 430074, Hubei, China
[2]China-EU Institute for Clean and Renewable Energy, Huazhong University of Science and Technology, Wuhan 430074, Hubei, China
[3]Institute of Nuclear and New Energy Technology, Tsinghua University, Beijing 100084, China

**Note:** This paper is part of the APL Special Collection on New Technologies and New Applications of Advanced Batteries.
[a)]**Authors to whom correspondence should be addressed:** wang-l@tsinghua.edu.cn and yongmingsun@hust.edu.cn

## ABSTRACT

Silicon (Si)-based anode is promising for the next-generation high-energy lithium-ion batteries due to the high capacity. However, it suffers parasitic side reactions between electrode and electrolyte in the initial cycle, which consumes abundant active lithium and makes it one of the limiting factors for the implementation of Si-based anodes. It is of vital importance to suppress the side reactions at the electrode interphase and improve the electrochemical/chemical stability. Here, we designed an ultrathin double-shell interphase structure (∼15 nm), consisting of an inner $VO_2$ nanoshell and an outer C nanoshell. The inner $VO_2$ nanolayer avoided the direct contact between active Si and electrolyte, and, thus, hindered the side reactions between them. The carbon nanolayer stabilized the $VO_2$ layer mechanically and improved the electronic conductivity of the anode materials. Thus, a thin solid electrolyte interphase was formed on the as-designed Si@$VO_2$@C surface, and high initial Coulombic efficiency (ICE) was realized. Notably, the Si@$VO_2$@C electrode exhibited a high reversible capacity of 2300 mAh $g^{-1}$ at 0.1 C and high ICE of 90.2%, which was about 18% higher than that of a pristine Si electrode. Also, the electrode displayed stable electrochemical cycling with high capacity retention of 84.8% for 100 cycles at 0.4 C. With 15 wt. % addition into the graphite, the hybrid electrode Si@$VO_2$@C/graphite exhibited a high reversible charge capacity of 596 mAh $g^{-1}$ and satisfactory cycling performance with high capacity retention of 83.8% at 100 mA $g^{-1}$ under a high area capacity of 3.46 mAh $cm^{-2}$, showing promise for the practical application.

Silicon (Si)-based anode has been widely regarded as a promising replacement for the-state-of-art graphite anode in lithium ion batteries (LIBs) to pursue higher energy density due to the much higher capacity (4200 mAh $g^{-1}$ for Si vs 372 mAh $g^{-1}$ for graphite) and suitable operation potential (∼0.45 V in average vs $Li^+/Li$) of Si.[1,2] Unfortunately, the practical implantation of a Si-based anode remains significantly challenging due to the inherent low conductivity (0.44 $\Omega^{-1}\,cm^{-1}$), dramatic volume change (∼400% from Si to $Li_{4.4}Si$), and parasitic interfacial side reactions between the active material and electrolyte during the cycling, the latter of which is highly undesired.[3–5] During the initial lithiation process, the electrochemical reduction of organic electrolyte takes place on the surface of Si to form a solid electrolyte interphase (SEI),[6–8] which consumes both abundant electrolyte and active $Li^+$ from the cathode, leading to low initial Coulombic efficiency (ICE).[9,10] The situation becomes even worse when taken into consideration of the large volume change, which was accompanied by the electrochemical lithiation/delithiation processes.[7,11,12]

Until now, various structures and composites have been explored to stabilize the interphase structure of the Si-based anode, including microscale Si/graphene composites,[9] watermelon-inspired Si/C microspheres,[13] and Si-based alloy composite.[14,15] These well-designed structures/composites could reduce the overall accessible area of active Si to electrolyte, suppressing the side reactions between them, and, thus, improve the ICE. On the other hand, electrolyte engineering has been well conducted to stabilize their interphase by regulating the electrode–electrolyte reactivity and their reaction products.[16,17] Typically, fluoroethylene carbonate (FEC) is widely accepted as an effective functional additive for the regular carbonate-based electrolytes, and it significantly increases the ratio of inorganic components in SEI and enhances its stability.[18,19] Some salts play a similar role in regulating the composition and structure of SEI and hinder the side reactions between the solvents of electrolyte and active materials, such as $LiNO_3$[20] and lithium bis(oxalato)borate (LiBOB).[21,22] An "electrolyte-phobic surface" design could reduce the direct contact between active materials and electrolyte, enabling suppressed side reactions at the interphase.[10] Meanwhile, the design of new polymeric binders with robust mechanical property has also turned out effective to prevent the fracture of Si particles and electrodes, and, thus, suppress their parasitic side reactions with electrolyte.[23,24] Despite these important progresses, the low ICE due to the large initial active Li loss is still an open question for the industrial application of Si-based anode. Here, we would like to regulate the electrode–electrolyte reactivity by functional interphase design to suppress the initial lithium loss, which is important but yet well explored in literatures.

Herein, we reported an ultrathin $VO_2$@C double-shell interphase design on Si(Si@$VO_2$@C) for suppressing the electrode–electrolyte reactions and improve the ICE of Si-based anode, which was fabricated through a simple ball milling with the combination of thermal annealing operation. The inner $VO_2$ nanolayer (∼10 nm) closely contacted with active Si avoided its direct contact with the electrolyte and reduced the decomposition of electrolyte and consumption of active Li. The outer C nanolayer (∼5 nm) mechanically supported the $VO_2$ layer and improved the electronic conductivity of the anode materials. As a result, the ICE of the product was much increased, and the cycling stability was significantly improved. The Si@$VO_2$@C electrode delivered high ICE of 90.2%, which was close to commercial graphite. Moreover, the Si@$VO_2$@C electrode showed significantly improved cycling stability with a capacity retention of 84.8% for 100 cycles at 0.4 *C* in sharp contrast to 46.5% for the pristine Si electrode.

The phase information of the pristine Si and Si@$VO_2$@C was measured by x-ray diffraction (XRD). As shown in Fig. 1(a), typical peaks of crystalline Si at 28.42°, 47.31°, and 56.10° (JCPDS 05–0565) were observed for the as-fabricated Si@$VO_2$@C, without showing any $VO_2$ peaks (Fig. S1, supplementary material). The XRD peaks for the pristine Si and Si@$VO_2$@C were highly overlapped, indicating that the synthesis process of the Si@$VO_2$@C did not cause any phase change of Si.[25] Thermogravimetric analysis (TG) was conducted in air atmosphere to measure the carbon content. According to the TG spectrum shown in Fig. 1(b), the weight of the Si@$VO_2$@C remained stable in the temperature range from 100 to 400 °C, and it gradually decreased from 400 to 550 °C. The carbon content of the Si@$VO_2$@C could be, thus, evaluated as ∼5.6 wt. %.[26] Scanning electron microscopy (SEM) images of the pristine Si and Si@$VO_2$@C were employed to reveal the morphology information. As shown in Figs. 1(c) and 1(d), irregular

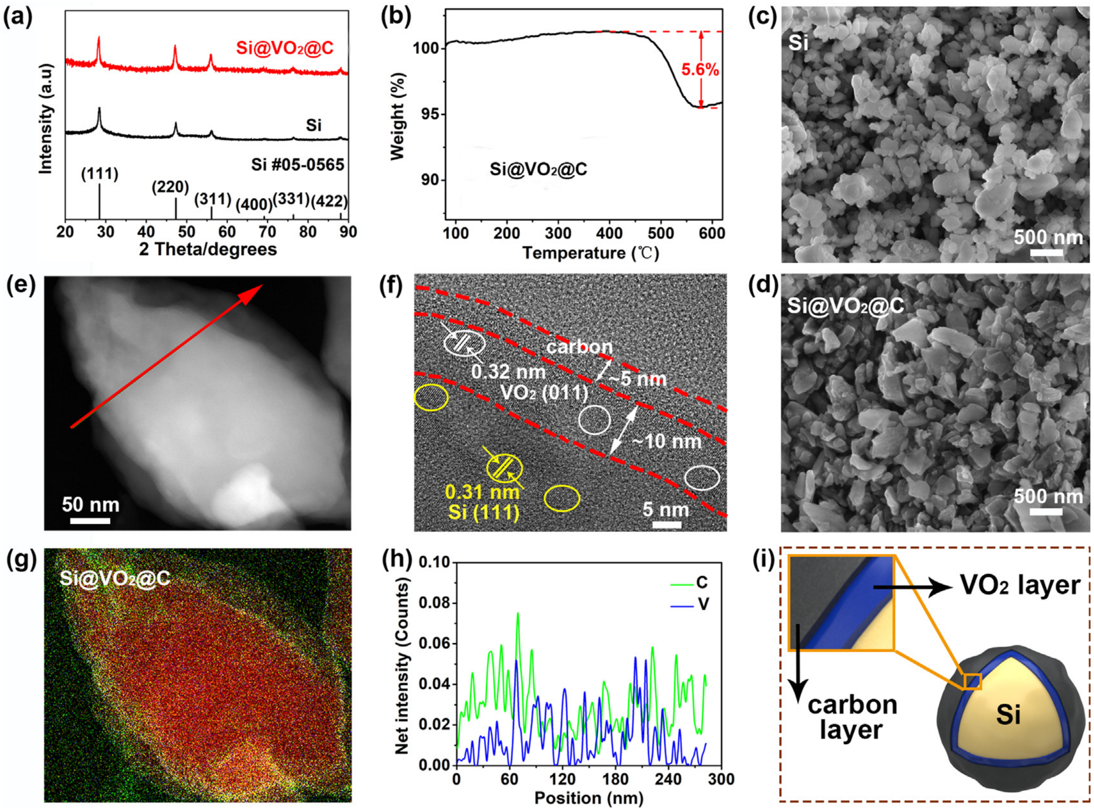

**FIG. 1.** Characterizations of the pristine Si and Si@$VO_2$@C. (a) XRD patterns of the pristine Si (bottom) and Si@$VO_2$@C (top). (b) TG curve of Si@$VO_2$@C. SEM images of (c) the pristine Si and (d) Si@$VO_2$@C. (e) Dark-field TEM image and (g) the corresponding EDS mapping image of Si@$VO_2$@C. Green, yellow, and red stand for C, V and Si, respectively. (f) High-resolution TEM image of Si@$VO_2$@C. (h) EDS count-position plot across the particle in (e). (i) Schematic of the double-shell interphase structure of Si@$VO_2$@C.

particles with size 200–800 nm were observed for both the pristine Si and Si@$VO_2$@C, indicating that the initial Si particles were well maintained during the construction of $VO_2$@C double-shell interphase.[27] Transmission electron microscopy (TEM) and EDS mapping measurements were further carried out to investigate the structure and the elemental distribution of Si@$VO_2$@C. The uniform distribution of $VO_2$ and C on the Si surface was confirmed in Figs. 1(e), 1(g), and S2, respectively. As shown in Fig. 1(f), high-resolution transmission electron microscopy (HRTEM) image showed a double-shell structure with a ∼10 nm-thick inner shell and a ∼5 nm-thick outer shell. The core of the measured particle showed typical lattice fringes of (111) Si with the spacing of 0.31 nm. Crystalline lattice fringes with interplanar spacings of 0.32 nm were observed in the inner shell, corresponding to (011) plane of $VO_2$, and the typical amorphous structure for hard carbon was shown in the outer shell, suggesting the successful construction of double layer nanoshell on Si core. Moreover, EDS counts of V and C signals across the particle were further recorded in Figs. 1(e) and 1(h), again verifying the successful construction of double-shell structure of $VO_2$@C. All the results above supported the successful construction of the double-shell protective structure of the $VO_2$@C on Si as illustrated in Fig. 1(i). Therefore, suppressed decomposition of electrolyte and reduced in active Li consumption could be expected during the initial electrochemical lithiation process.

The initial charge and discharge curves of the Si@$VO_2$@C and pristine Si electrodes were shown in Fig. 2(a). Slight increase in overpotential was observed for the Si@$VO_2$@C electrode in the charge process in comparison to the pristine Si electrode, which arose from the introduction of the double-shell $VO_2$@C interphase. The Si@$VO_2$@C electrode delivered high lithiation and delithiation capacities of 2645 and 2386 mAh $g^{-1}$ at the current density of 0.1 *C*, respectively, delivering impressive ICE of 90.2%. In contrast, the pristine Si electrode displayed lithiation and delithiation capacities of 3253 and 2359 mAh $g^{-1}$, showing much lower ICE of 72.5%, respectively. Note that 90.2% is an impressive ICE value for Si-based anode, which is close to that of commercial graphite electrode and is among the best records for Si-based anodes.[10,28–30] Meanwhile, the Si@$VO_2$@C electrode also showed higher ICE than the core–shell structured Si@$VO_2$ and Si@C electrodes (Fig. S3). These results highlighted the crucial role of $VO_2$@C double-shell on the Si nanoparticles in separating the active Si and electrolyte, reducing their parasitic side reactions during the initial electrochemical lithiation process, and, thus, improving the stability of the electrode interface.

The long-term electrochemical cycling was conducted for the Si@$VO_2$@C and pristine Si electrodes at 0.1 *C* for the initial five activation cycles and 0.4 *C* for the subsequent cycles, as shown in Fig. S4, Table S1, and Fig. 2(b). The charge capacity of the Si@$VO_2$@C

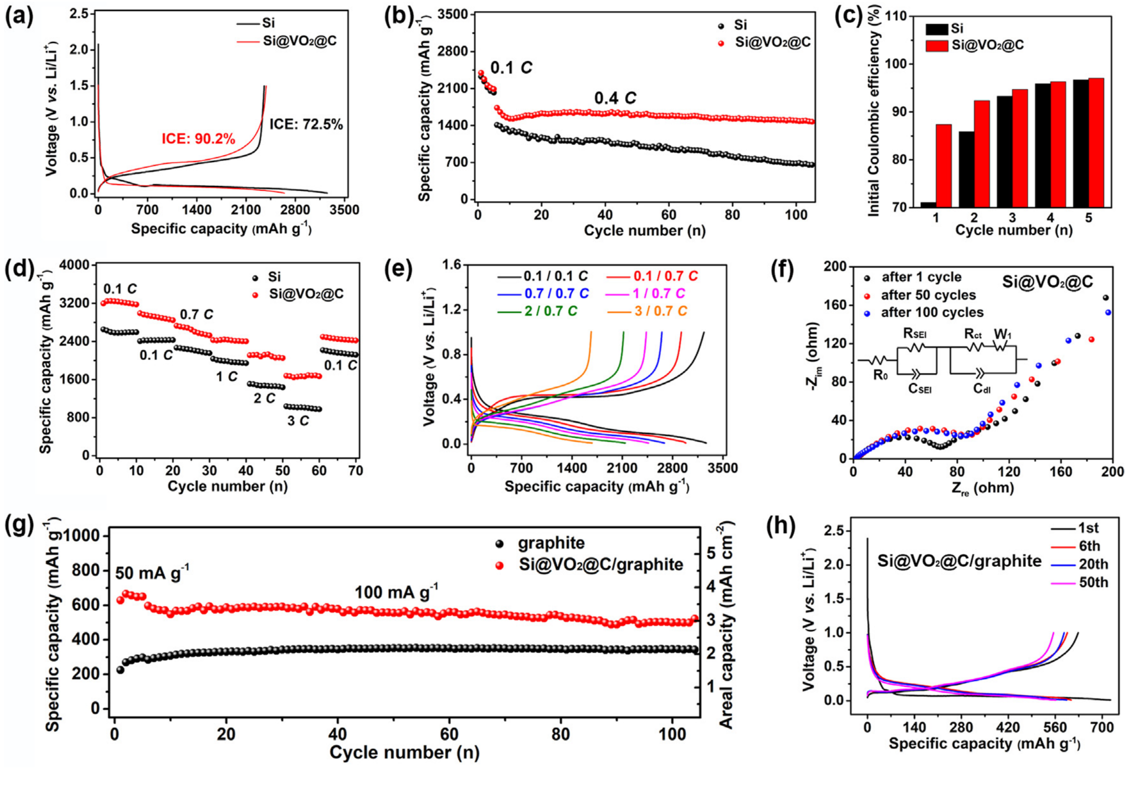

**FIG. 2.** Electrochemical performance of Si@$VO_2$@C. (a) The initial voltage-capacity profiles of pristine Si (black) and Si@$VO_2$@C (red) electrodes. (b) Electrochemical cycling performance of pristine Si (black) and Si@$VO_2$@C (red) electrodes at 0.4 *C*. (The electrodes were first activated at 0.1 *C* for five cycles before long-term cycling.) (c) Coulombic efficiency of pristine Si (black) and Si@$VO_2$@C (red) electrodes for the initial five cycles. (d) Rate performance of pristine Si (black) and Si@$VO_2$@C (red) electrodes at different *C* rates and (e) the corresponding voltage-capacity profiles of Si@$VO_2$@C electrode. (f) Nyquist plots of the Si@$VO_2$@C electrode after 1 (black), 50 (red), and 100 (blue) cycles and the equivalent circuit (insert). (g) Electrochemical cycling performance of the hybrid Si@$VO_2$@C/graphite and bare graphite electrodes at 100 mA $g^{-1}$ and (h) the corresponding voltage-capacity profiles of the hybrid Si@$VO_2$@C/graphite electrodes for the selected cycles.

electrode was 2398 mAh $g^{-1}$ for the first cycle, which was similar to the pristine Si electrode at 0.1 *C*. Slight capacity decay was observed for both electrodes in the initial five activation cycles. When the current density increased to 0.4 *C*, the Si@$VO_2$@C electrode and pristine Si electrode showed capacities of 1736 and 1411 mAh $g^{-1}$, respectively. Also, their capacity retentions for 100 cycles were 84.8% and 46.5%, respectively. These results suggested the advancement of the $VO_2$@C double-shell structure in enabling high reversible capacities under moderate current densities. It was obviously observed that the Si@$VO_2$@C electrode exhibited much less polarization in comparison to the pristine Si electrode according to their voltage–capacity curves (Fig. S5). Typically, the average charge voltages for the Si@$VO_2$@C and pristine Si electrodes were 0.24 and 0.3 V at the 50th cycle, respectively. As comparison, the electrochemical cycling performance of the Si@$VO_2$ and Si@C (Fig. S6) with core-shell structures was also carried out. Both the electrodes displayed better cycling performance than the pristine Si electrode but worse than the Si@$VO_2$@C electrode, supporting the significant effect of $VO_2$@C double-shell structure in stabilizing electrodes. Comparison in Coulombic efficiency between pristine Si and Si@$VO_2$@C electrodes for the initial five cycles was shown in Fig. 2(c). In addition to the first cycle, the Si@$VO_2$@C electrode exhibited higher Coulombic efficiency than the pristine Si electrodes on cycling. The average Coulombic efficiency was 93.6% and 88.6% for the Si@$VO_2$@C and pristine electrode for the initial five cycles, respectively, again indicating the double-shell of the Si@$VO_2$@C electrode in suppressing the undesirable side reactions between the active materials and electrolyte and reducing the active lithium loss.[31] The fast-charging capability of Si@$VO_2$@C and the pristine Si electrodes [Fig. 2(d)] were conducted at various lithiation rates from 0.1 to 3 *C* with a constant delithiation rate of 0.7 *C*. The Si@$VO_2$@C electrode exhibited reversible capacities of 2921, 2651, 2434, 2118, and 1667 mAh $g^{-1}$ at 0.1, 0.7, 1, 2, and 3 *C*, respectively [Fig. 2(e)]. The capacity retention reached 57% at 3 *C* (calculated based on the capacity at 0.1 *C*). In contrast, the pristine Si electrode showed capacity retention of 42% at the same test conditions. To further probe the effect of $VO_2$@C double-shell structure in stabilizing the electrode, the electrochemical impedance spectroscopy (EIS) on cycling was conducted [Figs. 2(f) and S7]. According to the Nyquist plots, the interphase resistance[32] of the Si@$VO_2$@C electrode showed slight increase from 75.4 to 99.8 Ω, in contrast to 90.4 to 135.2 Ω for pristine Si electrode from the first to 100th cycle. Note that the Nyquist plots of the Si@$VO_2$@C electrodes were highly overlapped, suggesting its stable interphase structure. Without the protection of $VO_2$@C shell, the pristine Si electrode showed gradually increase in interphase resistance from 50th to 100th cycle, due to the continuous accumulation of the resistive SEI on the electrode surface.[9,13]

In order to further explore the application of Si@$VO_2$@C in LIBs, 15 wt. % of Si@$VO_2$@C was mixed with 85 wt. % of graphite as the active material to prepare hybrid Si@$VO_2$@C/graphite electrode. As shown in Figs. 2(g) and 2(h), the hybrid Si@$VO_2$@C/graphite electrode with a mass loading of ∼6 mg $cm^{-2}$ showed a high reversible charge capacity of 628 mAh $g^{-1}$ and areal capacity of 3.65 mAh $cm^{-2}$ after the initial lithiation/delithiation process at the current density of 50 mA $g^{-1}$, which was about twice as that of bare graphite electrode with same mass loading. When the current density increased to 100 mA $g^{-1}$, the hybrid electrode still exhibited a high specific capacity of 596 mAh $g^{-1}$ and areal capacity of 3.46 mAh $cm^{-2}$, which were ∼1.5 times higher than that of the bare graphite. With such a high areal capacity similar to commercial anode in state-of-the-art lithium-ion batteries, the hybrid Si@$VO_2$@C/graphite electrode delivered a satisfactory cycling performance with a high capacity retention of 83.8% for 100 cycles. In addition, the electrochemical cycling performance of the full cell comprising Si@$VO_2$@C/graphite anode and $LiCoO_2$ cathode was tested. As shown in Fig. S8, the full cell displayed a high reversible discharge capacity of 153 mAh $g^{-1}$ at 0.2 *C* after five activation cycles at 0.1 *C* and showed high capacity ration of 82.4% at 0.2 *C* after 80 cycles, suggesting its promise for the practical application in next-generation high-energy lithium ion batteries.

To verify the improved electrochemical performance, the pristine Si and Si@$VO_2$@C electrodes after cycling have been investigated by X-ray photoelectron spectroscopy (XPS), SEM, and TEM. Figure 3(a) exhibited high-resolution Li 1s XPS spectra for the pristine Si and Si@$VO_2$@C after 1 lithiation/delithiation cycle. Peaks at 54.9, 56.0, and 56.9 eV were shown for both samples, which corresponded to $ROCO_2Li$, $Li_2CO_3$, and LiF of the SEI, respectively.[33] It is noted that the relative intensity for inorganic species on the Si@$VO_2$@C surface was much higher than that on the pristine Si surface, indicating the higher inorganic species in SEI of the Si@$VO_2$@C. The results of high-resolution F1s spectra also supported the higher content of LiF on the surface of Si@$VO_2$@C than pristine Si [Fig. 3(b)].[7] The content of inorganic species in SEI (such as LiF and $Li_2CO_3$) was thermodynamically stable, would effectively prevent penetration of electrolyte, and, thus, helps to realize stable Si-based electrode.[34] Therefore, the double-shell nanolayer design of $VO_2$@C on the surface of Si promoted the formation of inorganic-rich SEI, responsible for the superior electrochemical performance.[35,36] The organic-rich SEI layer was vulnerable and permeable by the electrolyte solution, leading to undesirable parasitic side reactions.[37–39] The serious side reactions and accumulated side products were responsible for instability of the pristine Si electrode [Figs. 3(c) and S9(a)]. In contrast, benefited from stable inorganic components of the SEI, the Si@$VO_2$@C electrode showed stable electrode structure after 1 full lithiation/delithiation cycle [Figs. 3(d) and S9(b)]. Figure 3(e) showed the dark-field TEM and the corresponding Si, V, and F elemental mapping images of Si@$VO_2$@C after one cycle. Intact particle with the well-maintained $VO_2$@C surficial layer was observed, suggesting the effect of $VO_2$@C double-shell interphase structure in stabilizing the active Si. The enhanced structure stability of the Si@$VO_2$@C with the inorganic-rich SEI layer explained the improved electrochemical performance.

In conclusion, an ultrathin double-shell interphase structure has been designed and fabricated successfully on Si, which consisted of an inner $VO_2$ nanoshell and an outer C nanoshell. Such interphase design suppressed the side reactions between active Si and electrolyte and promoted the formation of inorganic-rich SEI, which were responsible for the significantly improved ICE and satisfactory cycling performance. As expected, the Si@$VO_2$@C electrode exhibited a high ICE of 90.2% (18% higher than that of the pristine Si electrode) as well as stable electrochemical cycling with a capacity retention of 84.8% after 100 cycles. With 15 wt. % addition into commercial graphite, the hybrid Si@$VO_2$@C/graphite electrode exhibited a high reversible charge capacity of 596 mAh $g^{-1}$ at a high area capacity of 3.46 mAh $cm^{-2}$ and satisfactory cycling performance with capacity retention of 83.8%. The double-shell interphase

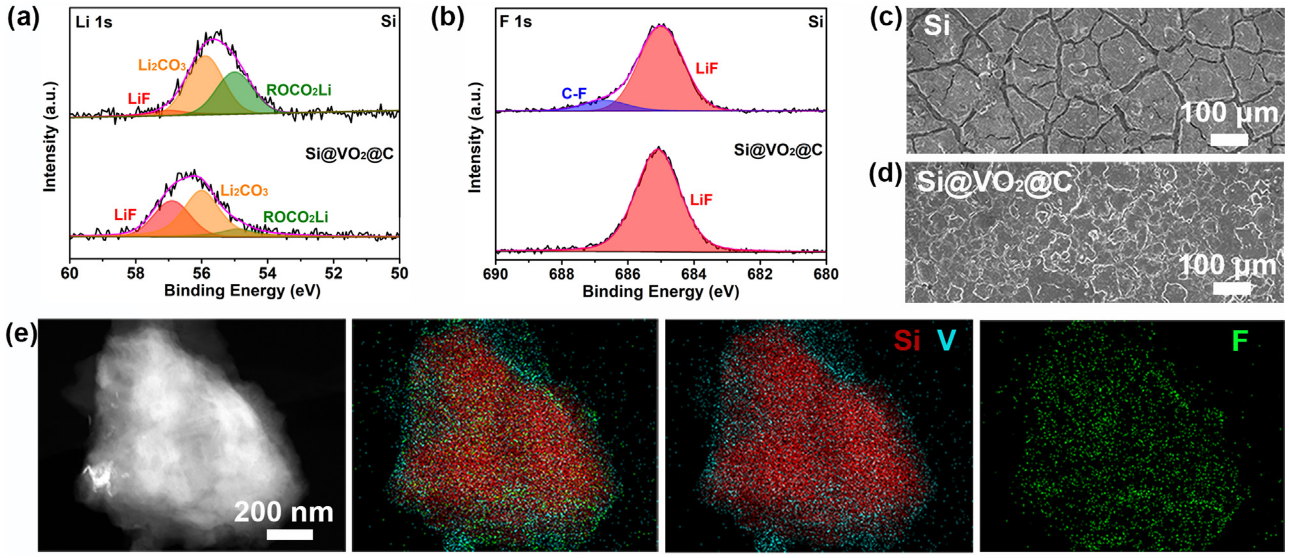

**FIG. 3.** Characterizations of Si@$VO_2$@C and pristine Si electrodes after one lithiation/delithiation cycle. (a) High-resolution Li 1s XPS spectra for pristine Si (top) and Si@$VO_2$@C (bottom) electrodes. (b) High-resolution F 1s XPS spectra for pristine Si (top) and Si@$VO_2$@C (bottom) electrodes. SEM images of (c) the pristine Si and (d) Si@$VO_2$@C electrodes. (e) Dark-field TEM image and elemental mapping images of the Si@$VO_2$@C.

structure represents a new pathway for the design of an advanced Si-based anode with respect to suppressing the side reactions on materials interphase and improving the ICE.

See the supplementary material for the experimental section, including materials preparation, materials characterizations, and electrochemical characterizations.

This work was financially supported by the Natural Science Foundation of China (Grant No. 52072137) and the Innovation Fund of Wuhan National Laboratory for Optoelectronics of Huazhong University of Science and Technology. The authors would like to thank the Analytical and Testing Center of Huazhong University of Science and Technology (HUST) for providing the facilities to conduct the characterizations.

## AUTHOR DECLARATIONS

### Conflict of Interest

The authors have no conflicts to disclose.

### Author Contributions

**Xiaoxue Chen:** Data curation (equal); Visualization (equal); Writing – original draft (equal). **Zihe Chen:** Visualization (supporting). **Yang Ni:** Data curation (supporting). **Li Wang:** Writing – review & editing (equal). **Yongming Sun:** Supervision (lead); Writing – review & editing (lead).

## DATA AVAILABILITY

The data that support the findings of this study are available within the article and its supplementary material.

## REFERENCES

[1] D. Wang, C. Zhou, B. Cao, Y. Xu, D. Zhang, A. Li, J. Zhou, Z. Ma, X. Chen, and H. Song, Energy Storage Mater. **24**, 312 (2020).
[2] S. Pan, J. Han, Y. Wang, Z. Li, F. Chen, Y. Guo, Z. Han, K. Xiao, Z. Yu, M. Yu, S. Wu, D. W. Wang, and Q. H. Yang, Adv. Mater. **34**, 2203617 (2022).
[3] C. Stetson, M. Schnabel, Z. Li, S. P. Harvey, C. S. Jiang, A. Norman, S. C. DeCaluwe, M. Al-Jassim, and A. Burrell, ACS Energy Lett. **5**, 3657 (2020).
[4] D. H. S. Tan, Y.-T. Chen, H. Yang, W. Bao, B. Sreenarayanan, J.-M. Doux, W. Li, B. Lu, S.-Y. Ham, B. Sayahpour, J. Scharf, E. A. Wu, G. Deysher, H. E. Han, H. J. Hah, H. Jeong, J. B. Lee, Z. Chen, and Y. S. Meng, Science **373**, 1494 (2021).
[5] Y. Chen, L. Yang, F. Guo, D. Liu, H. Wang, J. Lu, J. Zheng, X. Yu, and H. Li, J. Power Sources **527**, 231178 (2022).
[6] Z. Chen, A. Soltani, Y. Chen, Q. Zhang, A. Davoodi, S. Hosseinpour, W. Peukert, and W. Liu, Adv. Energy Mater. **12**, 2200924 (2022).
[7] B. Q. Xiong, X. Zhou, G. L. Xu, Y. Liu, L. Zhu, Y. Hu, S. Y. Shen, Y. H. Hong, S. C. Wan, X. C. Liu, X. Liu, S. Chen, L. Huang, S. G. Sun, K. Amine, and F. S. Ke, Adv. Energy Mater. **10**, 1903186 (2019).
[8] X. Zhang, S. Weng, G. Yang, Y. Li, H. Li, D. Su, L. Gu, Z. Wang, X. Wang, and L. Chen, Cell Rep. Phys. Sci. **2**, 100668 (2021).
[9] Y. Li, K. Yan, H. W. Lee, Z. Lu, N. Liu, and Y. Cui, Nat. Energy **1**, 15029 (2016).
[10] C. Qian, J. Zhao, Y. Sun, H. R. Lee, L. Luo, M. Makaremi, S. Mukherjee, J. Wang, C. Zu, M. Xia, C. Wang, C. V. Singh, Y. Cui, and G. A. Ozin, Nano Lett. **20**, 7455 (2020).
[11] Y. He, L. Jiang, T. Chen, Y. Xu, H. Jia, R. Yi, D. Xue, M. Song, A. Genc, C. Bouchet-Marquis, L. Pullan, T. Tessner, J. Yoo, X. Li, J. G. Zhang, S. Zhang, and C. Wang, Nat. Nanotechnol. **16**, 1113 (2021).
[12] Y. Sun, N. Liu, and Y. Cui, Nat. Energy **1**, 16071 (2016).
[13] Q. Xu, J.-Y. Li, J.-K. Sun, Y.-X. Yin, L.-J. Wan, and Y.-G. Guo, Adv. Energy Mater. **7**, 1601481 (2017).
[14] W. Li, J. Liao, X. Li, L. Zhang, B. Zhao, Y. Chen, Y. Zhou, Z. Guo, and M. Liu, Adv. Funct. Mater. **29**, 1903638 (2019).
[15] W. Li, X. Li, J. Liao, B. Zhao, L. Zhang, L. Huang, G. Liu, Z. Guo, and M. Liu, Energy Environ. Sci. **12**, 2286 (2019).
[16] J. Chen, X. Fan, Q. Li, H. Yang, M. R. Khoshi, Y. Xu, S. Hwang, L. Chen, X. Ji, C. Yang, H. He, C. Wang, E. Garfunkel, D. Su, O. Borodin, and C. Wang, Nat. Energy **5**, 386 (2020).

[17] Y. Jin, N. H. Kneusels, L. E. Marbella, E. Castillo-Martinez, P. Magusin, R. S. Weatherup, E. Jonsson, T. Liu, S. Paul, and C. P. Grey, J. Am. Chem. Soc. **140**, 9854 (2018).

[18] V. Etacheri, O. Haik, Y. Goffer, G. A. Roberts, I. C. Stefan, R. Fasching, and D. Aurbach, Langmuir **28**, 965 (2012).

[19] Y. Jin, B. Zhu, Z. Lu, N. Liu, and J. Zhu, Adv. Energy Mater. **7**, 1700715 (2017).

[20] W. Qi, L. Ben, H. Yu, W. Zhao, G. Zhao, and X. Huang, Prog. Nat. Sci.: Mater. Int. **30**, 321 (2020).

[21] S. Dalavi, P. Guduru, and B. L. Lucht, J. Electrochem. Soc. **159**, A642 (2012).

[22] N.-S. Choi, K. H. Yew, H. Kim, S.-S. Kim, and W.-U. Choi, J. Power Sources **172**, 404 (2007).

[23] Y. K. Jeong and J. W. Choi, ACS Nano **13**, 8364 (2019).

[24] Y. Cho, J. Kim, A. Elabd, S. Choi, K. Park, T. W. Kwon, J. Lee, K. Char, A. Coskun, and J. W. Choi, Adv. Mater. **31**, e1905048 (2019).

[25] S. Yang, K. Yamamoto, X. Mei, A. Sakuda, T. Uchiyama, T. Watanabe, T. Takami, A. Hayashi, M. Tatsumisago, and Y. Uchimoto, ACS Appl. Energy Mater. **5**, 667 (2022).

[26] X. Sun, J. Gao, C. Wang, X. Gao, J. Liu, N. Gao, H. Li, Y. Wang, and K. Yu, Chem. Eng. J. **383**, 123198 (2020).

[27] L. Lin, Y. Ma, Q. Xie, L. Wang, Q. Zhang, and D. L. Peng, ACS Nano **11**, 6893 (2017).

[28] Y. Tzeng, C. Y. Jhan, Y. C. Wu, G. Y. Chen, K. M. Chiu, and S. Y. Guu, Nanomaterials (Basel) **12**, 1387 (2022).

[29] Z. Xiao, C. Yu, X. Lin, X. Chen, C. Zhang, H. Jiang, R. Zhang, and F. Wei, Nano Energy **77**, 105082 (2020).

[30] W. Zhang, S. Fang, N. Wang, J. Zhang, B. Shi, Z. Yu, and J. Yang, Inorg. Chem. Front. **7**, 2487 (2020).

[31] X. Chen, G. Ge, W. Wang, B. Zhang, J. Jiang, X. Yang, Y. Li, L. Wang, X. He, and Y. Sun, Sci. China Chem. **64**, 1417 (2021).

[32] G. Zheng, Y. Xiang, L. Xu, H. Luo, B. Wang, Y. Liu, X. Han, W. Zhao, S. Chen, H. Chen, Q. Zhang, T. Zhu, and Y. Yang, Adv. Energy Mater. **8**, 1801718 (2018).

[33] W. Huang, Y. Wang, L. Lv, W. Wang, C. Jin, G. Zhu, Q. Shi, Q. Qu, C. Jin, and H. Zheng, Energy Storage Mater. **42**, 493 (2021).

[34] J. Tan, J. Matz, P. Dong, J. Shen, and M. Ye, Adv. Energy Mater. **11**, 2100046 (2021).

[35] M. Baek, J. Kim, J. Jin, and J. W. Choi, Nat. Commun. **12**, 6807 (2021).

[36] M. He, R. Guo, G. M. Hobold, H. Gao, and B. M. Gallant, Proc. Natl. Acad. Sci. U. S. A. **117**, 73 (2020).

[37] S. J. An, J. Li, C. Daniel, D. Mohanty, S. Nagpure, and D. L. Wood III, Carbon **105**, 52 (2016).

[38] J. D. McBrayer, M.-T. F. Rodrigues, M. C. Schulze, D. P. Abraham, C. A. Apblett, I. Bloom, G. M. Carroll, A. M. Colclasure, C. Fang, K. L. Harrison, G. Liu, S. D. Minteer, N. R. Neale, G. M. Veith, C. S. Johnson, J. T. Vaughey, A. K. Burrell, and B. Cunningham, Nat. Energy **6**, 866 (2021).

[39] Y. Zhou, M. Su, X. Yu, Y. Zhang, J. G. Wang, X. Ren, R. Cao, W. Xu, D. R. Baer, Y. Du, O. Borodin, Y. Wang, X. L. Wang, K. Xu, Z. Xu, C. Wang, and Z. Zhu, Nat. Nanotechnol. **15**, 224 (2020).